Radio Over Fiber Downlink Design for Spatial Modulation and Multi-Set Space-Time Shift-Keying

Yichuan Li* *Student Member, IEEE*, Ibrahim A. Hemadeh* *Student Member, IEEE*, Mohammed El-Hajjar* *Senior Member, IEEE*, Lajos Hanzo* *Fellow, IEEE*

*School of ECS, University of Southampton, UK

Abstract—**Spatial Modulation (SM) and Multi-Set Space-Time Shift-Keying (MS-STSK) are capable of striking a flexible design trade-off between the multiplexing and diversity gains attained. These techniques can also be combined with beamfoming for the sake of supporting reliable millimeter wave (mmWave) communications. In this treatise, we propose an analogue Radio over Fiber (RoF) downlink network relying on SM and MS-STSK combined with beamforming and up-conversion to mmWave carrier frequencies, whilst using all-optical processing. In the proposed Analogue RoF (A-RoF) system, most of the digital processing of the baseband SM and MS-STSK is carried out by the Central Unit and the implicitly carried bits of SM/MS-STSK, such as the antenna index selection and dispersion matrix selection bits, are recovered by the remote radio head (RRH) of our A-RoF network for creating a multi-functional Multiple-Input Multiple-Output (MIMO) arrangement. As detailed in [1], the classic modulated bits are conveyed by the radio signal, without requiring any additional Analogue-to-Digital Conversion (ADC) and Digital-to-Analogue Conversion (DAC) before transmission from the antennas. Moreover, A-RoF-aided techniques are invoked for achieving optical processing aided beamforming and optical up-conversion to a mmWave carrier frequency. Thus, we invoke A-RoF techniques for the generation of our SM/MS-STSK signal with the aid of optically up-converted millimetre wave beamforming without using any electronic oscillators, mixers or phase shifters. Furthermore, our A-RoF-aided system's BER performance is similar to the conventional all-electronic SM/MS-STSK scheme.**

Index terms SM, MS-STSK, Radio over Fiber, Beamforming, Millimetre wave.

I. INTRODUCTION

As a result of the popularity of flawless multimedia services supported by the ubiquitous smartphones, cellular networks are approaching their capacity, especially in densely populated areas [2], [3]. Small cells are capable of overcoming the network capacity shortage with the aid of adding more cells of high-quality wireless coverage having a small cell radius [4]–[6]. Analogue Radio over Fiber (A-RoF) techniques are capable of supporting small cell deployment using centralized processing, where the small cell base-stations (BS) are connected using fiber [5] and only optical-to-electronic (O-E) conversion and RF amplification are required at the small-cell base station [7], [8]. A simplified schematic of the A-RoF-aided small cell system is shown in Figure 1, where a single central unit (CU) supports several remote small-cell radio ports. This architecture is potentially capable of reducing

the overall cost of the network [7], [9]. As shown in Figure 1, the central unit is responsible for centralized digital processing, while the remote radio heads are used for radio transmission, including the O-E conversion, filtering, amplifications and then transmission from the transmitter antenna arrays (TAAs). **This architecture is also applicapable to the popular cloud radio access networks (C-RAN) [10], [11], where a central office carries out all the baseband signal processing [12], serving multiple low-complexity and low-cost remote radio heads (RRHs). The A-RoF transmissions [5], [13] to the RRHs invoked by C-RAN [14] are also capable of supporting the emerging small-cell technologies [14], [15].**
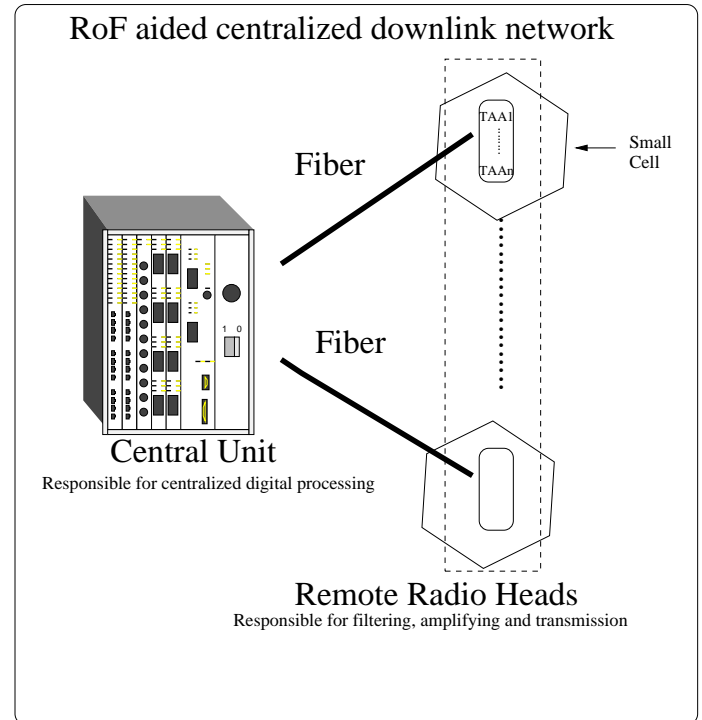

Figure 1: **A-RoF system architecture for centralized digital processing. The Central Unit performs centralized digital processing and radio modulation, while the Remote Radio Head carries out filtering, amplification and radio transmission.**

Moreover, Millimeter Wave (mmWave) carries frequencies as naturally suitable for small cells owing to the associated short propagation range, thus reducing the inter-cell interference [2], [16]. However, traditional all-electronic mmWave processing requires high-frequency Radio Frequency (RF) mixers, which tend to degrade the link's performance [17]. We circumvent this problem with the aid of A-RoF techniques by

Nomenclature

A-RoF	Analogue RoF
AC	Antenna Combination
ADC	Analogue-to-Digital Conversion
AoD	Angle of Departure
AWGN	Additive White Gaussian Noise
BER	Bit Error Ratio
BLAST	Bell Lab's Layer Space-Time
BPSK	Binary Phase Shift Keying
BS	Base-Station
C-RAN	Cloud Radio Access Network
CFBG	Chirped Fiber Bragg Grating
CU	Central Unit
DAC	Digital-to-Analogue
DAA	Demodulation and Antenna Arrangement
DSF	Dispersion-shifted Fiber
EBPF	Electronic Band Pass Filter
EDFA	Erbium-doped Fiber Amplifier
FBG	Fiber Bragg Grating
LD	Laser Diode
MIMO	Multiple-Input-Multiple-Output
ML	Maximum Likelihood
mmWave	Millimeter Wave
MS-STSK	Multi-set Space Time Shift Keying
MZM	Mach-Zehnder Modulator
OBPF	Optical Band Pass Filter
OC	Optical Circulator
ODSB	Optical Double Side-Band
O-E	Optical-to-electronic
OIL	Optical Interleaver
PD	Photo-detector
PRBS	Pseudorandom Binary Sequence
QAM/PSK	Quadrature Amplitude Modulation/ Phase Shift Keying
QPSK	Quadrature Phase Shift Keying
RF	Radio Frequency
RoF	Radio over Fiber
RRH	Remote Radio Head
SINR	Signal-to-Interference-plus-Noise Ratio
SM	Spatial Modulation
SNR	Signal-to-noise Ratio
STBC	Space Time Block Code
STSK	Space Time Shift Keying
TAA	Transmitter Antenna Arrays

List of Symbols

$\hat{x}_1$	Implicit bits
$\hat{x}_2$	Classic modulated bits
x_1	Implicit symbols
x_2	Classic modulated symbols
f_{RF}	RF frequency for radio carrier modulation
f_{drive}	Drive frequency of MZM
λ_n	Optical Wavelengths
V_π	MZM switching voltage
V_{dr}	MZM drive voltage
ω_{LO}	Angular center frequency of MZM drive signal
ω_{RF}	Angular center frequency of f_{RF}
J_n	The Bessel functions of the first kind and order n
E_{in}	Input optical signal of MZM
E_{MZM}	Output optical signal of MZM
P_{laser}	LD's output power
ω_{oc}	Optical carrier's angular frequency
N_t	Number of transmitter antennas
N_r	Number of receiver antennas
M	STSK space dimension
Q	Number of dispersion matrix
T	STSK time slots
$\mathcal{L}$	PSK/QAM constellation size
B_1	Antenna selection bits of MS-STSK
B_2	Dispersion matrices selection bits of MS-STSK
B_3	Classic modulated bits of MS-STSK

dispensing with high frequency mixers and demonstrate that optical upconversion to mmWave frequencies are capable of outperforming its all-electronic counterpart [17], by exploiting the Mach-Zehnder Modulator's (MZM's) non-linearity, the fiber's non-linearity and the photo-detector's non-linearity for optical up-conversion [17]. **Moreover, multi-frequency mmWave wavelength up-conversion techniques using four-wave mixing in a semiconductor optical amplifier has been proposed in [18], [19], which aim for improving the capacity and for reducing the interchannel interference. Additionally, photonic generation of multiple-frequency mmWave signals using tunable optical frequency combs has been presented in [20] for mitigating the crosstalk between the various optical network units involved. Fur-**

thermore, a combination of De-multiplexers and MZMs in a passive optical network [21] has been proposed for supporting the photonic generation of 60/120 GHz signals. By contrast, in this treatise we exploit the MZM's non-linearity combined with an Optical Interleaver (OIL) for optical upconversion and scalable beamforming.

On the other hand, as a key technique of reducing the inter-channel interference and of increasing the Signal-to-Interference-plus-Noise Ratio (SINR) of mmWaves, beamforming may be invoked to compensate for the short propagation range of mmWave communications and hence for achieving an SINR gain [22]. Furthermore, A-RoF aided beamforming relying on all-optical processing is capable of substantially reducing the complexity of our multi-functional Multiple-Input Multiple-Output (MF-MIMO) configuration, which is designed to combine the gains of spatial diversity, multiplexing and beamforming techniques, by avoiding the employment of phase shifters used in traditional electronic beamforming [13].

Let us now elaborate a little further on Spatial Modulation (SM) [23], which is a low-cost MIMO technique, where one out of M transmit antennas is activated to transmit a single classic Quadrature Amplitude Modulation/Phase Shift Keying (QAM/PSK) symbol. Hence, in SM, in addition to the classic modulated bits, $log_2 M$ implicit antenna index based information bits are conveyed [1] [24]. SM is capable of striking a compelling trade-off between Bell Lab's Layered Space-Time (BLAST) and Alamouti's Space-Time Block Code (STBC), whilst relying on a reduced number of RF chains. Its further benefits are its ability to use a single-antenna based Maximum Likelihood (ML) detection scheme and the mitigation or elim-

---

[1]We refer to the antenna selection index in SM as the implicit information.

ination of inter-channel interference [25], [26]. Additionally, Space-Time-Shift-Keying (STSK) constitutes a generalization of SM, where one out of say M number of dispersion matrices is activated for implicitly conveying $log_2 M$ bits, which can attain both diversity and multiplexing gains [26], [27]. Based on intrinsincally amalgamating the philosophy of both SM and STSK, the concept of Multi-Set STSK (MS-STSK) was proposed in [28] as a further generalized architecture, which is capable of striking a beneficial design trade-off between the achievable multiplexing and diversity gains [28].

In A-RoF system's downlink, RF signals are transmitted over the optical fiber from the central unit to the remote radio head, where the centralized baseband processing is carried out. Then, the photo detected signal is transmitted by the antennas without the need for electronic processing in the baseband, such as modulation, DAC or ADC [5], [17]. In this paper, we propose a RoF system relying on centralized processing aided SM and MS-STSK combined with all-optical beamforming, while simultaneously achieving optical up-conversion to mm-Wave carrier frequencies.

In the proposed A-RoF network, the SM and MS-STSK information is modulated onto the two side-bands of an optically modulated signal in the central unit of Figure 1, which is up-converted from a frequency of 3 GHz to a mmWave frequency by pure optical processing utilising a MZM and an OIL. The side-band containing the implicit information[2] is decoded by the remote radio head of Figure 1. Furthermore, tunable optically aided beamforming can be achieved using optical Fiber Bragg Grating (FBG), which introduces a linear relationship between the time delays and the optical wavelengths by reflecting different wavelengths from different locations inside the FBG discussed in [22], [29]. Moreover, the SM/MS-STSK signals are transmitted over a Dispersion-Shifted Fiber (DSF), which exibits a low dispersion in our proposed wavelength region [30]. This is used for mitigating the dispersion effects imposed on the optical fiber aided beamforming.

Thus, compared to a conventional cellular architecture, where the RF and baseband signal processing are integrated into a base station [9], our proposed design is capable of concentrating the digital baseband processing in the central unit. Hence the complexity of the remote radio head is reduced to that of low-cost filtering, switching and amplification [31]. Against the above backdrop, the novel contributions of this paper are summarised as follows:

1) **Intelligent centralized-processing aided A-RoF network design**: We propose a sophisticated A-RoF network for supporting low-complexity SM or MS-STSK combined with all-optical beamforming and up-conversion to mmWave carrier frequencies. More explicitly, all-optical SM/MS-STSK processing is combined with beamforming in the mmWave spectral band. To the best of our knowledge, this is the first time that optical fiber aided analogue beamforming using CFBG is conceived for mmWave communications.

2) **Optical processing aided SM/MS-STSK encoding scheme**: We propose an architecture for carrying both implicit antenna-index-based information and classically

modulated information by SM/MS-STSK intrinsically amalgamated with optical processing. Again, this avoids the ADC and RF carrier modulation at the remote radio head. Instead, an optically up-converted mmWave signal carries the SM and MS-STSK symbols, which are then fed into linear uniform arrays for beamforming, hence requiring no additional electronic signal processing at the remote radio heads.

The rest of the paper is organised as follows. Section II presents the A-RoF aided SM encoding network, where the conventional electronic SM scheme and the proposed model are presented and discussed. Then, in Section III, the A-RoF aided MS-STSK scheme is introduced and analyzed, followed by our conclusions in Section IV.

II. A-RoF NETWORK DESIGN FOR SM

In this paper, we propose an all-optical processing aided Multi-Functional MIMO (MF-MIMO) [32] system, where SM/MS-STSK, optical upconversion and optical fiber aided beamforming were amalgamated. In A-RoF networks, most of the digital processing is carried out in the central unit of Figure 1. In this contribution, we propose a novel A-RoF network carrying SM symbols, which can be used both for the mobile fronthaul or backhual.

In the proposed network, after the conventional electronic SM encoding, the SM information is transmitted over the dispersion-shifted fiber, where the signal is up-converted to a mmWave carrier frequency and linearly time-delayed signals are attained with the aid of FBGs for achieving an angularly selective beamforming effect. In this section, we first present the conventional SM electronic encoding design and then we discuss the proposed system architecture and its performance.

A. Conventional electronic SM encoding scheme

Figure 2 shows the conventional SM encoding process using N_t transmit antennas, where the input bits are partitioned into two streams. The first stream is used for activating one out of the N_t transmit antennas, while the second stream is used for modulating a classical QAM/PSK symbol[3], as shown in Figure 2. Hence, the transmitted symbol implicitly carries the selected antenna index information.
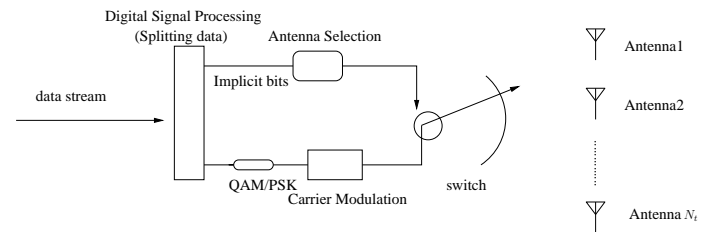
Figure 2: **Conventional electronic SM encoding scheme used by the Base Stations of the conventional cellular architecture.**

In the traditional architecture, SM encoding is carried out at each BS, adding extra cost and complexity to the small-cell

---

[2]In MS-STSK, the implicit information refers to the antenna selection index and dispersion matrix index information.

[3]In our paper, we term data symbol for transmission as classic modulated symbol.

system [9]. By contrast, in our proposed design, the digital processing is concentrated to the central unit, as detailed in the following sections. To elaborate a little further, our proposed A-RoF-aided SM design is capable of confining the SM encoding to a single central unit, hence substantially easing the burden imposed on small-cell base stations.

B. Proposed A-RoF-aided SM Design

Upon introducing optical fiber aided beamforming and optical up-conversion, our system transmits the SM symbols using a mmWave carrier and all-optical processing, relying on the remote radio heads of Figure 1. Figure 3 and 4 highlight the operation of our A-RoF aided SM system and the corresponding spectral-domain manipulations. In the following, we will detail the signal processing in our system of Figure 3, while referring to the corresponding spectral-domain manipulations seen in Figure 4[4].

SM encoding: Similar to the conventional electronic SM encoding scheme, a pseudorandom binary sequence (PBRS) is generated and split into two streams that convey the antenna selection bits $\hat{x}_1$ as well as the classic modulated bits $\hat{x}_2$. Then, as shown in Figure 3, we map the implicit antenna-index bits to a $2^L - QAM/PSK$ scheme, where 2^L represents the number of transmitter antenna elements of each antenna array of Figure 3. Similarly, the classic modulated bits are conveyed by $2^M - QAM/PSK$ symbols according to the system requirements. Note in the interest of explicit clarity that in contrast to the conventional electronic SM encoding scheme, in our amalgamated optical/RF system both SM streams are conveyed by QAM/PSK symbols over the fiber. This ensures that they have the same symbol rate during their transmission in the A-RoF link. For example, if a PRBS block of the bits $b_1...b_3$ is transmitted, b_1, b_2 are used for the implicit antenna-index bits as $\hat{x}_1$ for activating one out of four antenna elements, while b_3 is used for classic Binary Phase Shift Keying (BPSK) modulated bits for optical transmission as $\hat{x}_2$. To ensure that b_3 is conveyed by the b_1, b_2-based antenna element after the A-RoF link, b_1, b_2 are conveyed by a Quadrature Phase Shift Keying (QPSK) symbol.

Afterwards, both types of SM symbols are carried by a RF frequency of f_{RF} and fed into a pair of LDs for direct modulation, as shown in Figure 3. The two LDs are directly modulated by x_1 and x_2 to generate a pair of wideband signals, respectively, as shown at ① and ② of Figure 4. Then, the left side-band of ① carrying x_1 and the right side-band of ② carrying x_2 are retained by the Optical Band Pass Filters (OBPFs) and combined to a new ODSB signal using **an optical combiner**, as shown in Figure 3 and marked by ③ of Figure 4.

Thus, SM encoding relies on Optical Double Side-band (ODSB) modulation associated with an RF frequency of f_{RF}, where both the implicit symbols x_1 used for antenna selection and the classic modulated symbols x_2 are mapped to one of the side-bands, each using a combination of Laser Diodes (LDs) and OBPFs.

mmWave optical upconversion: Afterwards, optical modulation is employed using the Mach-Zenhder Modulator (MZM) of Figure 3, where, as demonstrated at ④ of Figure 4, the

drive voltage of the MZM can be appropriately tuned in order to copy the ODSB signal carrying x_1 and x_2 to multiple wavelengths. This will result in multi-wavelength signals that can be transmitted over mmWaves, by beneficially exploiting the MZM's non-linearity [13] [5]. Then, the multi-wavelength ODSB signal is transmitted over a DSF at the zero-dispersion wavelength in the vicinity of 1550 nm [30], for the sake of mitigating the dispersion effects, whilst aiming for a constant time-delay. As shown in Figure 3, optical up-conversion is applied using an optical interleaver, as illustrated in Figure 5. The multi-wavelength signal at the fiber's output is fed into the OIL, where the two outputs of Figure 5 provide the beat frequencies representing the mmWave frequency carrying x_2 and the RF frequency f_{RF} carrying x_1, respectively. **For example, if a multi-wavelenth signal of the ODSBs having the center frequencies of λ_1, λ_2 and λ_3, shown in Figure 5 is fed into the OIL, Port 1 of the OIL retains the optical carrier and the left side-band of λ_2 as well as the right side-bands of λ_1 and λ_3 while Port 2 outputs the remaining spectrum. The OIL acts as a periodic filter, which splits the spectrum for generating a set of appropriately beating frequencies after the PDs of the 'Beamforming and SM signal mapping' block of Figure 3, generating the RF and mmWave frequencies in our proposed system. Generally, Port 1 retains the optical carrier and the left side-bands of λ_{2n} as well as the right side-bands of λ_{2n-1}, while Port 2 outputs the right side-bands of λ_{2n} as well as the optical carrier and the left side-bands of λ_{2n-1}.** The corresponding spectra of Port 1 and Port 2 are shown at ⑤ and ⑥ of Figure 4.

Beamforming and SM signal mapping: Following the OIL, the antenna selection bits $\hat{x}_1$ are recovered after passing the signal gleaned at Port 1 of Figure 3 through the OBPF, Photo Detection (PD), Electronic Band Pass Filter (EBPF), baseband demodulation and the ADC components, **where the OBPF retains the spectrum of ⑦ of Figure 4, the PD achieves the O-E conversion, the EBPF obtains the f_{RF} RF signal and the ADC converts the analogue RF signal to digital symbols for SM switching.** The photo-detected RF signal used for antenna selection appears at f_{RF}. On the other hand, the output of Port 2 is fed into a tunable chirped FBG, which imposes a linear time delay on each wavelength by reflecting different wavelength from different locations.

The time-delayed multi-wavelength signal carrying x_2 is then transmitted by the activated antenna, where the photo-detectors of the Demodulation and Antenna Arrangement (DAA) block of Figure 3 receive the corresponding time-delayed wavelengths and then convert them to a mmWave signal having a frequency of $(f_{RF} + f_{drive})$. Therefore, the mmWave signals of the DAA associated with the linear time delays are passed on to the corresponding Transmitter Antenna Array (TAA), whose index has been decoded after the photo detection stage of Figure 3.

More specifically, as shown in Figure 4, the spectra at ① and ② represent the directly modulated ODSB optical signals of the LDs of Figure 3, where x_1 and x_2 are mapped to the

---

[4]The circled numbers of Figure 3 correspond to the numbers in Figure 4

[5]In Figure 4, we portrayed the comb-like signals for the sake of showing the spectral evolution in our system design in a stylized format. In fact, the amplitude of the corresponding wavelengths relies on both the harmonics' order and on the switching voltage as well as on the amplitude of the MZM's drive voltage, which will be analyzed in Section II-B1
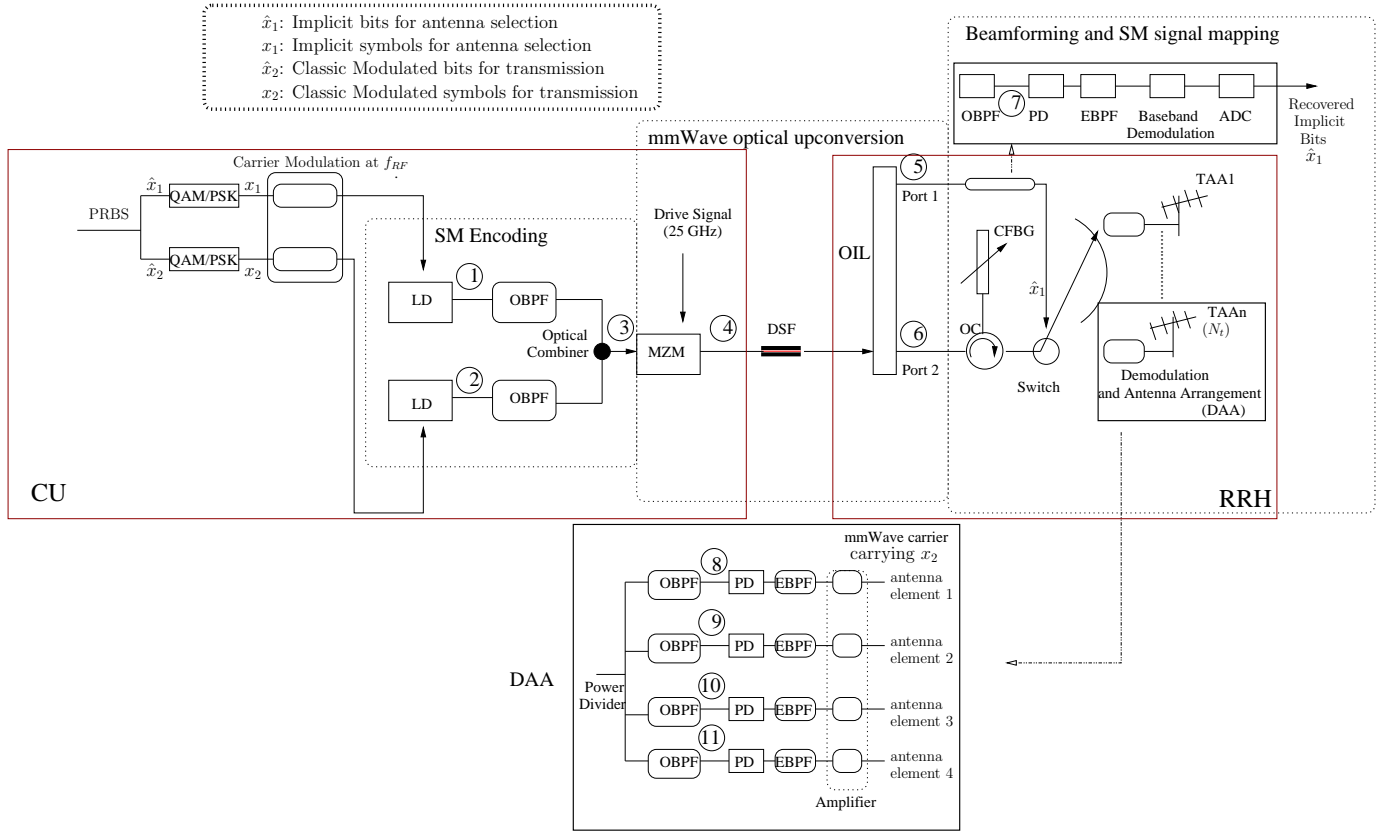
Figure 3: **A centralized A-RoF aided SM encoding scheme. The CU performs digital modulation, carrier modulation, E-O conversion and SM encoding, while the RRH implements the radio functions (filtering, O-E conversion, photo-detection, amplifying and radio transmission), as well as SM implicit data recovery and SM switching.**

side-bands having a center frequency of f_{RF}. Then, following the appropriate filtering by the OBPF after each LD of Figure 3, we obtain a new ODSB, with x_1 being mapped to the left and x_2 to the right side-band, as shown at ③ of Figure 4. The ODSB signal is then converted to a multi-wavelength signal by beneficially exploiting the MZM's non-linearity of Figure 3, resulting in the spectra at ④ of Figure 4. The OIL of Figure 3 is then used for appropriately filtering the spectrum to be utilised for mmWave generation and antenna-index bit recovery. The stages ⑤ and ⑥ show the spectrum of port 1 and port 2 of Figure 3, where the corresponding frequencies will be processed in order to form stages ⑦, ⑧, ⑨, ⑩ and ⑪ of Figure 4. The photo-detected RF signal after stage ⑦ is used for antenna selection, while those of ⑧, ⑨, ⑩ and ⑪ are used for mmWave signal generation. The details of these spectral shaping operations will be discussed in the following sections.

In contrast to the conventional SM encoding scheme of Figure 2, our proposed system is capable of carrying the SM symbols encapsulated in a multi-wavelength optical signal over the optical fiber. At the fiber's output, the implicit antenna index bits are recovered, while the corresponding classic modulated symbols are modulated by a up-converted mmWave signal. Our design eliminates the need for both the ADC and the DAC at the remote radio head, which substantially reduces the cost and complexity of the remote radio head. The optically up-converted and beamformed mmWave signal can be directly

fed into the TAA, without any additional electronic processing for modulation and demodulation, where the electronic filters and amplifiers are used for ensuring that the amplitudes of the mmWave signals emitted from each TAA element are appropriately adjusted. In the following, we detail both the rationale and mathematical model of our system regarding mmWave generation and beamforming.

1) mmWave Generation: As presented in the middle dashed box of Figure 3, the MZM and OILs contribute to the mmWave signal generation. The harmonics generated by the MZM's nonlinearity result in multiple wavelengths, where each wavelength carries a copy of the ODSB signal of ③ of Figure 4[6]. Assuming that E_{in} is the ODSB input of the MZM, as detailed in [33], higher-order optical side-bands are generated relying on the voltage of the drive signal imposed on the MZM. The resultant optical signal is given by:

$$
\begin{aligned}
E_{MZM}(t) &= cos[\pm\frac{\pi}{4} + \frac{\pi V_{dr}cos(\omega_{LO})}{2V_\pi}]E_{in}(t) \\
&= \frac{E_{in}(t)}{\sqrt{2}}[J_0(\frac{\pi|V_{dr}|}{2V_\pi}) + 2\sum_{n=1}^{\infty}(-1)^n J_{2n}(\frac{\pi V_{dr}}{2V_\pi})cos(2n\omega_{LO}t) \\
&\quad \pm 2\sum_{n=1}^{\infty}(-1)^n J_{2n-1}(\frac{\pi V_{dr}}{2V_\pi})cos((2n-1)\omega_{LO}t)],
\end{aligned}
$$

(1)

where the E_{MZM} is the output field of the MZM with a switching voltage of V_π, which induces a phase-shift of π for each arm, while V_{dr} is the drive voltage of the angular center frequency of $\omega_{LO}/(2\pi)$. Here, $J_n(\frac{\pi V_{dr}}{2V_\pi})$ is the Bessel
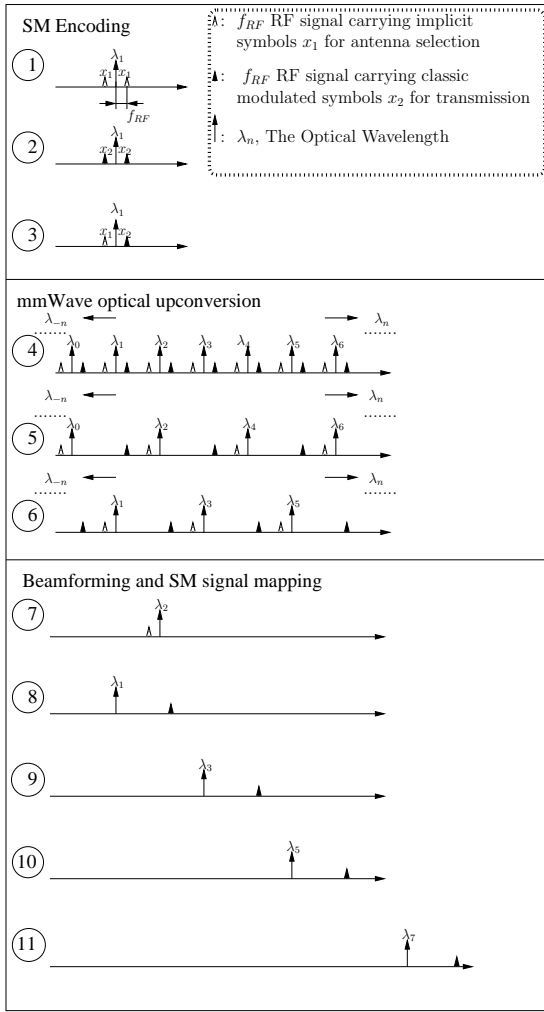
[6]λ_1 of Figure 4 is the LD's optical carrier

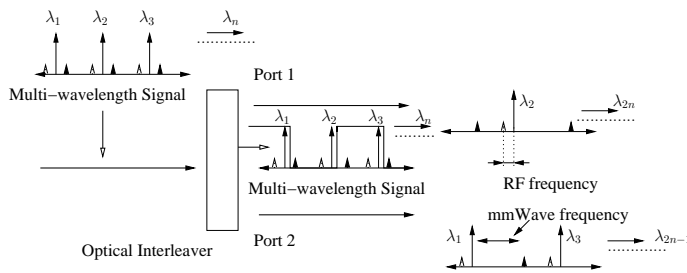Figure 4: Spectral-domain charaterization of proposed system of Figure 3

Figure 5: An optical interleaver

function of the first kind and order n, which determines both **the number and the amplitude of the side-bands**.

The resultant multi-wavelength ODSB signal carrying the RF of ω_{RF} is then fed into the OIL of Figure 3, after transmission over the optical fiber, where the OIL removes some of the multi-wavelength signal frequencies. Explicitly, in the case of Port 2 of the OIL of Figure 3, λ_1 associated with the left side-band, λ_3 with the right side-band as well as the right side band of λ_2 and λ_4 are filtered out, as shown at ⑤ of Figure 4. In this case, the beat frequency between λ_1 and the right side-band of λ_3 is photo-detected, which generates a frequency of $\omega_{RF} + \omega_{LO}$, namely 28 GHz in our design and completes the mmWave frequency generation.

The up-converted frequency relies on the frequency ω_{rf} of the drive voltage imposed on the MZM of Figure 3, which can be appropriately tuned in order to up-convert the signal to any desired frequency in the mmWave spectrum.

More specifically, if a RF signal of center frequency of 3 GHz is directly modulated by the LDs of Figure 3, a multi-wavelength ODSB signal carrying a 3 GHz RF signal is then generated with the aid of a MZM's drive signal of 25 GHz, resulting in a wavelength spacing of 25 GHz among the neighbouring λ_n components. Then, as shown in stages ④, ⑤ and ⑥ of Figure 4, the OIL of Figure 3 removes some of the frequencies output by Port 1 and Port 2 of the OIL. Thus, on one hand, the output signal of Port 1 is filtered by the OBPF seen at ⑦ of Figure 3. Then, after processing by the Beamforming and SM signal mapping block of Figure 3, the beat frequency becomes 3 GHz, which is used for the implicit bits recovery of SM. On the other hand, following the transmission of the output signal of Port 2 of the OIL in the CFBG scheme of Figure 3 for beamforming, the signal is fed into the DAA of Figure 3, resulting in the time-delayed signals of stages ⑧, ⑨, ⑩ and ⑪ of Figure 3. After the PD, the beat frequency obtained is the up-converted mmWave frequency of 28 GHz. The beamforming scheme will be further detailed in the next section.

2) Beamforming: Due to the short mmWave propagation range, we exploit our optical signal processing aided beamforming scheme to extend the propagation range of mmWave communications. In our design, beamforming is introduced by exploiting the constant time-delay difference between the neighbouring antenna elements of each transmitter, where the constant time delay difference is obtained with the aid of CFBG, which impose different time-delays on different wavelengths due to their different locations of reflection [29]. Furthermore, CFBG supports true-time delay based beamforming for wideband signals, which is achieved by avoiding the beam-squinting introduced by the popular phase shifting based beamforming scheme [22].

The signal generated at the output of the OIL of Figure 3 is transmitted to an optical circulator (OC), which is a three-port component, where the time-delayed multi-wavelength signals reflected by CFBG are forwarded to one of the DAA block of Figure 3. The time delay introduced by CFBG is linearly proportional to the transmitting wavelengths, which can be translated to a specific beamsteering direction [34]. Furthermore, the reflected frequency spectrum of the CFBG can be appropriately tuned to control the time delay, thus adjusting the beamsteering direction [35]. Subsequently, the output of the OC is split into several branches shown in the DAA block of Figure 3. As shown at ⑧, ⑨, ⑩, ⑪ of Figure 4, the desired wavelength is retained with the aid of optical BPF in DAA of Figure 3. Thus, each branch outputs the carrier associated with the same symbol but different delays. After the PD and electronic BPF of the DAA of Figure 3, the delayed carriers are fed into the antenna array elements, which can be translated into different beamforming patterns according to the appropriately tuned time delay differences. We will demonstrate that our system is capable of both mmWave carrier generation and beamforming with aid of the CFBG-induced time-delay as detailed mathematically in the

following section.

C. Mathematical Model of Multi-wavelength Signal Beam-forming

Since the time-delay imposed by the CFBG is applied in the optical domain, there may be a delay-difference between the modulated optical signal and its corresponding photo-detected beat signal. In this section, we show mathematically that the time-delay differences between the photo-detected RF signals of the neighbouring antennas remain constant. As mentioned in Section II-B, the RF signal is directly modulated by LDs and the input optical field of the MZM of Figure 3 is formulated as:

$$E_{in}(t) = \sqrt{P_{Laser}}e^{j\omega_{oc}t}[1 + cos(\omega_{RF}t)], \qquad (2)$$

where P_{Laser} is the LD's output power and ω_{oc} denotes the optical carrier's angular frequency corresponding to λ_1 of Figure 4. The MZM output field expressed in Equation (1) can be combined with Equation (2) to arrive at:

$$
\begin{aligned}
&E_{MZM}(t)\\
&= cos(\pm\frac{\pi}{4} + \frac{\pi V_{dr}cos(\omega_{LO})}{2V_\pi})E_{in}(t)\\
&= \frac{\sqrt{P_{laser}}[1+cos(\omega_{RF}t)]e^{j\omega_{oc}t}}{\sqrt{2}}[J_0(\frac{\pi|V_{dr}|}{2V_\pi})\\
&+2\sum_{n=1}^\infty(-1)^nJ_{2n}(\frac{\pi V_{dr}}{2V_\pi})cos(2n\omega_{LO}t)\\
&\pm2\sum_{n=1}^\infty(-1)^nJ_{2n-1}(\frac{\pi V_{dr}}{2V_\pi})cos((2n-1)\omega_{LO}t)]\\
&= \frac{\sqrt{P_{laser}}e^{j\omega_{oc}t}}{\sqrt{2}}[J_0(\frac{\pi|V_{dr}|}{2V_\pi})][1 + cos(\omega_{RF}t)]\\
&+2\sum_{n=1}^\infty(-1)^nJ_{2n}(\frac{\pi V_{dr}}{2V_\pi})[cos(2n\omega_{LO}t)\\
&+\frac{cos((2n\omega_{LO}+\omega_{RF})t)+cos((2n\omega_{LO}-\omega_{RF})t)}{2}]\\
&\pm2\sum_{n=1}^\infty(-1)^nJ_{2n-1}(\frac{\pi V_{dr}}{2V_\pi})[cos((2n-1)\omega_{LO}t)\\
&+\frac{cos(((2n-1)\omega_{LO}+\omega_{RF})t)+cos(((2n-1)\omega_{LO}-\omega_{RF})t)}{2}]\\
&= \frac{\sqrt{P_{laser}}}{\sqrt{2}}[J_0(\frac{\pi|V_{dr}|}{2V_\pi})[e^{j\omega_{oc}t} + e^{j(\omega_{oc}+\omega_{RF})t}/2\\
&+e^{j(\omega_{oc}t-\omega_{RF}t)}/2] + 2\sum_{n=1}^\infty(-1)^nJ_{2n}(\frac{\pi V_{dr}}{2V_\pi})\\
&\times[e^{j(\omega_{oc}+2n\omega_{LO})t}/2 + e^{j(\omega_{oc}-2n\omega_{LO})t}/2\\
&+\frac{e^{j(\omega_{oc}+2n\omega_{LO}+\omega_{RF})t}/2+e^{j(\omega_{oc}-2n\omega_{LO}-\omega_{RF})t}/2}{2}\\
&+\frac{e^{j(\omega_{oc}+2n\omega_{LO}-\omega_{RF})t}/2+e^{j(\omega_{oc}-2n\omega_{LO}+\omega_{RF})t}/2}{2}]\\
&\pm2\sum_{n=1}^\infty(-1)^nJ_{2n-1}(\frac{\pi V_{dr}}{2V_\pi})\\
&\times[\frac{e^{j(\omega_{oc}+(2n-1)\omega_{LO})t}+e^{j(\omega_{oc}-(2n-1)\omega_{LO})t}}{2}\\
&+\frac{e^{j(\omega_{oc}+(2n-1)\omega_{LO}+\omega_{RF})t}/2+e^{j(\omega_{oc}-(2n-1)\omega_{LO}-\omega_{RF})t}/2}{2}\\
&+\frac{e^{j(\omega_{oc}+(2n-1)\omega_{LO}-\omega_{RF})t}/2+e^{j(\omega_{oc}-(2n-1)\omega_{LO}+\omega_{RF})t}/2}{2}].
\end{aligned}
\tag{3}
$$

Thus, after the OIL and the DAA block of Figure 3, we arrive at multiple mmWave signals of the same frequency but having different time-delays. Here, the signal at the output of Port 2 after the OIL block of Figure 3 can be expressed from Equation (4) as follows:

$$
\begin{aligned}
&E_{IL_{bottom}}(t)\\
&= \frac{\sqrt{P_{laser}}}{\sqrt{2}}[J_0(\frac{\pi|V_{dr}|}{2V_\pi})(\frac{e^{j(\omega_{oc}-\omega_{RF})t}}{2} + e^{j\omega_{oc}t})\\
&+2\sum_{n=1}^\infty(-1)^nJ_{2n}(\frac{\pi V_{dr}}{2V_\pi})\\
&(\frac{e^{j(\omega_{oc}-2n\omega_{LO}-\omega_{RF})t}+e^{j(\omega_{oc}+2n\omega_{LO}-\omega_{RF})t}}{4}\\
&+\frac{e^{j(\omega_{oc}+2n\omega_{LO})t}+e^{j(\omega_{oc}-2n\omega_{LO})t}}{2})\\
&\pm2\sum_{n=1}^\infty(-1)^nJ_{2n-1}(\frac{\pi V_{dr}}{2V_\pi})\\
&\frac{e^{j(\omega_{oc}-(2n-1)\omega_{LO}+\omega_{RF})t}+e^{j(\omega_{oc}+(2n-1)\omega_{LO}+\omega_{RF})t}}{4}].
\end{aligned}
\tag{4}
$$

After the OIL, the beat frequency can be obtained by the DAA block seen at the bottom of Figure 3, where the right side-band of even wavelength (λ_2 and λ_4...) and its neighbouring wavelengths' optical carrier (λ_1 and λ_3...) are retained and

mapped to each line of the DAA block, as shown in Figure 4. Thus, assuming that no time-delay scheme is applied, the resultant photo-detected signal of the top line of the DAA block of Figure 3 is given as follows:

$$
\begin{aligned}
&E_{PD}(t)\\
&\propto |E_{IL}(t)|^2\\
&= |\frac{\sqrt{P_{laser}}}{\sqrt{2}}[J_0(\frac{\pi|V_{dr}|}{2V_\pi})\frac{e^{j\omega_{oc}t}}{2} \mp 2J_1(\frac{\pi V_{dr}}{2V_\pi})\\
&\frac{e^{j(\omega_{oc}+\omega_{LO}+\omega_{RF})t}}{2}]|^2\\
&= \frac{P_{laser}}{8}[J_0^2(\frac{\pi|V_{dr}|}{2V_\pi}) + 4J_1^2(\frac{\pi V_{dr}}{2V_\pi}) \mp 4J_0(\frac{\pi V_{dr}}{2V_\pi})J_1(\frac{\pi V_{dr}}{2V_\pi})\\
&\times cos(\omega_{LO} + \omega_{RF})t].
\end{aligned}
\tag{5}
$$

In order to achieve the desired beamforming effect, having an identical time-delay difference between neighbouring wavelengths is required. Thus, in terms of the first line of DAA shown in Figure 3, which feed the signal to antenna element 1 of each TAA, the CFBG applies the time-delay t_1 to the optical carrier λ_1 and t_2 to λ_2's right side-band x_2 upon introducing $\Delta t = t_2 - t_1$. The corresponding photo-detected beat signal is expressed as follows:

$$
\begin{aligned}
&E_{PD_{delayed}}(t)\\
&\propto |E_{IL_{delayed}}(t)|^2\\
&= |\frac{\sqrt{P_{laser}}}{\sqrt{2}}[J_0(\frac{\pi|V_{dr}|}{2V_\pi})\frac{e^{j\omega_{oc}(t-t_1)}}{2} \mp 2J_1(\frac{\pi V_{dr}}{2V_\pi})\\
&\frac{e^{j(\omega_{oc}+\omega_{LO}+\omega_{RF})(t-t_2)}}{2}]|^2\\
&= \frac{P_{laser}}{8}[J_0^2(\frac{\pi|V_{dr}|}{2V_\pi}) + 4J_1^2(\frac{\pi V_{dr}}{2V_\pi}) \mp 4J_0(\frac{\pi V_{dr}}{2V_\pi})J_1(\frac{\pi V_{dr}}{2V_\pi})\\
&\times cos((\omega_{LO} + \omega_{RF})(t - t_2) + \omega_{oc}(t_1 - t_2))]\\
&= \frac{P_{laser}}{8}[J_0^2(\frac{\pi|V_{dr}|}{2V_\pi}) + 4J_1^2(\frac{\pi V_{dr}}{2V_\pi}) \mp 4J_0(\frac{\pi V_{dr}}{2V_\pi})J_1(\frac{\pi V_{dr}}{2V_\pi})\\
&\times cos((\omega_{LO} + \omega_{RF})(t - t_2 - \frac{\omega_{oc}\Delta t}{\omega_{LO}+\omega_{RF}}))].
\end{aligned}
\tag{6}
$$

Similarly, assuming that the delay t_3 is applied to the optical carrier λ_3 of ⑥ of Figure 4 , while t_4 to the right side-band of λ_4 and that $\Delta t = t_2 - t_1 = t_4 - t_3$, the photo-detected signal of the second line of DAA block of Figure 3, which is fed into the antenna element 2 of each TAA of Figure 3 becomes:

$$
\begin{aligned}
&E_{PD_{delayed_2}}(t)\\
&\propto |\frac{\sqrt{P_{laser}}}{\sqrt{2}}[-2J_2(\frac{\pi V_{dr}}{2V_\pi})\frac{e^{j(\omega_{oc}+2\omega_{LO})(t-t_3)}}{2} \pm 2J_3(\frac{\pi V_{dr}}{2V_\pi})\\
&\frac{e^{j(\omega_{oc}+3\omega_{LO}+\omega_{RF})(t-t_4)}}{2}]|^2\\
&= \frac{P_{laser}}{8}[4J_2^2(\frac{\pi|V_{dr}|}{2V_\pi}) + 4J_3^2(\frac{\pi V_{dr}}{2V_\pi}) \mp 8J_2(\frac{\pi V_{dr}}{2V_\pi})J_3(\frac{\pi V_{dr}}{2V_\pi})\\
&\times cos((\omega_{LO} + \omega_{RF})(t - t_4) + (\omega_{oc} + 2\omega_{LO})(t_3 - t_4))]\\
&= \frac{P_{laser}}{8}[4J_2^2(\frac{\pi|V_{dr}|}{2V_\pi}) + 4J_3^2(\frac{\pi V_{dr}}{2V_\pi}) \mp 8J_2(\frac{\pi V_{dr}}{2V_\pi})J_3(\frac{\pi V_{dr}}{2V_\pi})\\
&\times cos((\omega_{LO} + \omega_{RF})(t - t_4 - \frac{(\omega_{oc}+2\omega_{LO})\Delta t}{\omega_{LO}+\omega_{RF}}))].
\end{aligned}
\tag{7}
$$

Thus, following the same philosophy, the photo-detected signal of third line of DAA of Figure 3 is,

$$
\begin{aligned}
&E_{PD_{delayed_3}}(t)\\
&\propto \frac{P_{laser}}{8}[4J_4^2(\frac{\pi|V_{dr}|}{2V_\pi}) + 4J_5^2(\frac{\pi V_{dr}}{2V_\pi}) \mp 8J_4(\frac{\pi V_{dr}}{2V_\pi})J_5(\frac{\pi V_{dr}}{2V_\pi})\\
&\times cos((\omega_{LO} + \omega_{RF})(t - t_6 - \frac{(\omega_{oc}+4\omega_{LO})\Delta t}{\omega_{LO}+\omega_{RF}}))],
\end{aligned}
\tag{8}
$$

where the delay t_5 is applied to the optical carrier λ_5 of ⑥ of Figure 4, while t_6 is applied to the right side-band of λ_6 and $\Delta t = t_2 - t_1 = t_4 - t_3 = t_6 - t_5$.

By comparing Equations (6), (7) and (8), it becomes clear that there exists some delay between each photo-detected output signal and for antenna element of each DAA, the delay will not be exactly the same. However, the time delay

difference of the photo-detected signals fed into neighbouring antenna elements of the DAA block of Figure 3 will be constant. Specifically, due to the linear relationship between the time-delay and the wavelengths, we obtain $\Delta t = t_2 - t_1 = t_4 - t_3 = t_6 - t_5$ and $t_2 - t_4 = t_4 - t_6$. The time-delay difference of the output signals between antenna element 1 and antenna element 2 of the DAA block of Figure 3 is $(t_4 - t_2) + \frac{2\omega_{LO}\Delta t}{\omega_{LO}+\omega_{RF}}$, while for antenna element 2 and antenna element 3 is $(t_6 - t_4) + \frac{2\omega_{LO}\Delta t}{\omega_{LO}+\omega_{RF}}$. Thus, the time difference remains constant for each neighbouring antenna element of each TAA of Figure 3.

Hence, we have shown mathematically that our beamforming signal generation is capable of maintaining a constant time-delay difference between the neighbouring photo-detected mmwave frequencies fed into different antenna elements. Thus, our all-optical design is capable of supporting beamforming, while simultaneously implementing mmWave upconversion.

D. Beamforming Simulation Results

In our system, a 30 mm CFBG is used for introducing the delay required at the different wavelengths in order to support beamsteering. The time-delay imposed on the different wavelengths when the total chirp of the grating period of CFBG is set to 1.05 nm, which represents the difference between first period and the last period in the CFBG. Our simulations were carried out by using the OPTGRATING software and the delay vs wavelength and frequency is shown in Figure 6, where the wavelength range spans from 1549 nm to 1551 nm.

Thus, the spectral width, which is refered to as the spectral range of reflected wavelength and changes with the total chirp [36], determines the time-delay difference as a function of frequency spacing. Proposed by [36], the total spectral width as well as total chirp can be adjusted by tuning a supported beam's deflection, resulting in a linear time-delay difference vs spectral width.

Furthermore, as analysed in Section II-C, the CFBG facilitates a constant time-delay difference of $(t_4 - t_2) + \frac{2\omega_{LO}\Delta t}{\omega_{LO}+\omega_{RF}}$, where Δt is the time-delay difference for a 28 GHz spacing and a time-delay difference $t_4 - t_2$ at a 50 GHz spacing. Thus, according to the linear relationship seen in Figure 6 and 7, the time-delay difference between the adjacent antenna elements is 77.6 ps, when a total chirp of 1.05 nm is applied. Then, by changing the total chirp of the tunable CFBG of Figure 3, we obtain the corresponding relationship between the total chirp and the time-delay difference regarding our design as shown in Figure 7, where the time-delay difference range spans from 77.6 ps to 40.6 ps, when increasing the total chirp from 1.05 nm to 2.05 nm with a step-size of 0.05 nm. Then, according to the time-delay difference range, we obtain a beam coverage range of almost 360°, as shown in Figure 8.

E. System Simulation Results and Discussions

In this section we analyse the performance of our SM system employing A-RoF combined with all-optical beamforming and up-conversion to mmWave frequency. **We compare our proposed system to the conventional SM system operating without A-RoF in the context of a single-RRH for verifying**
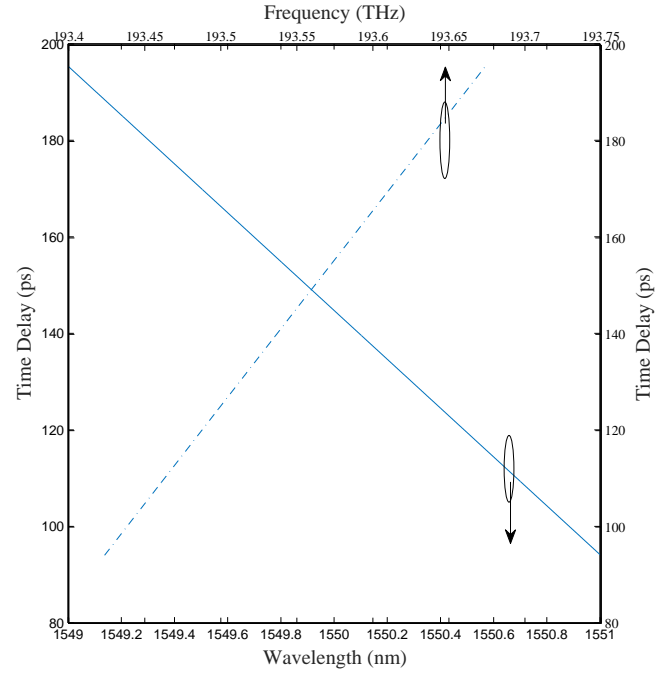

Figure 6: Linear Time Delay vs Wavelength and Frequency of CFBG with the total chirp of 1.05 nm
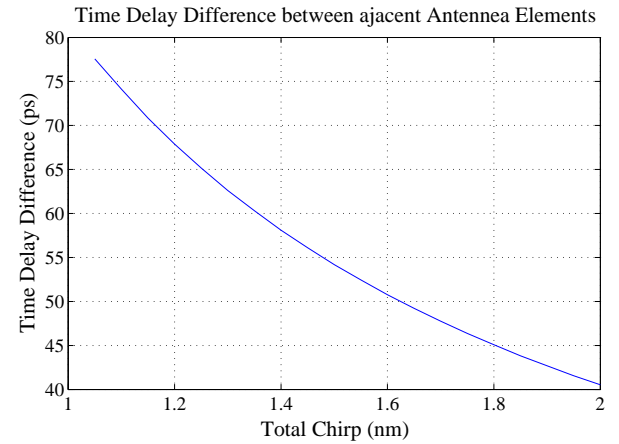

Figure 7: Total Chirp vs Time Delay Difference

our centralized design philosophy, which only imposes an almost negligible performance degradation. However, before discussing the results, let us first consider the MIMO channel model after the fiber transmission and study its effect on the system's performance.

In conventional MIMO systems employing N_t transmit antennas and N_r receive antennas, we model the received signal using $\mathbf{Y} = \mathbf{HX} + \mathbf{n}$, where $\mathbf{Y}$ represents the received symbol vector of size $(N_r \times 1)$, $\mathbf{H}$ is the MIMO channel matrix of size $(N_r \times N_t)$, $\mathbf{X}$ denotes the transmitted symbol vector of size $(N_t \times 1)$ and $\mathbf{n}$ is a $(N_r \times 1)$-element Additive White Gaussian Noise (AWGN) vector. However, during its fiber-based transition, the symbol vector $\mathbf{X}$ is affected by the fiber impairments, such as fiber attenuation, chromatic dispersion and fiber non-linearity in addition to the noise imposed by photo-detection [30]. Hence, in our system we model the SM based MIMO transmission after fiber-based transmission as
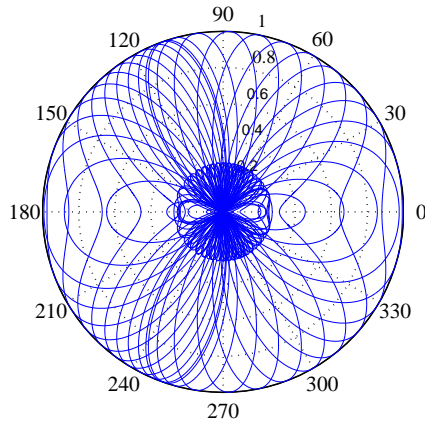
Beamforming with N=4 antenna arrays

Figure 8: Beamforming Pattern

Table I: Simulation Parameter

Parameter	Value
Bit rate	2 Gbps (2-antenna SM)
	3 Gbps (4-antenna SM)
RF signal	3 GHz
LD Center Wavelength	1550 nm
LD Power	1 mW
Drive Frequency (MZM)	25 GHz
Achieved mmWave frequency	28 GHz
MZM mode	push-pull mode
Fiber type	DSF
Fiber length	10 km
Channel Model	Split-Step Fourier Method
Modulation Type	BPSK
Wireless Channel	Rayleigh Fading Channel
Wireless Detection	ML Detection
Beamforming Type	4 Antenna Elements
Simulation Environment	MATLAB

follows:

$$\mathbf{Y} = \mathbf{H}\alpha\mathbf{X} + \mathbf{n}, \tag{9}$$

where α includes the effect of the fiber impairments and optical noise, while $\mathbf{n}$ includes the effect of the AWGN imposed by the RF circuits. Note that the channel state information now includes the wireless channel fading as well as the fiber impairments and these are jointly estimated at the receiver. In other words, the receiver will estimate $\mathbf{H}\alpha$.

Furthermore, in the proposed system, the beamsteering direction has to be known at the transmitter and this problem has been widely discussed in the literature, where several accurate Angle of Departure (AoD) estimation techniques have been proposed [37], [38]. Based on the above-mentioned design, we simulated our A-RoF network and compared the Bit Error Ratio (BER) of the received signal to that of its equivalent electronic SM counterpart dispensing with A-RoF transmission. Table I summarizes the parameters used in our system, **The bit rate given is the joint bit rate of implicit bits and classic modulated bits, where, for example, a classic modulated BPSK scheme of 1 Gbps can achieve a joint bit rate of 2 Gbps for two-antenna SM and 3 Gbps for four-antenna SM. The MS-STSK scheme applies the bit rate similarly, which is detailed in [39].**

An RF signal having a 3 GHz carrier is directly modulated by the LDs of Figure 3, while a drive frequency of 25 GHz is used by the MZM. This allows up-converting the 3 GHz signal to a mmWave signal of 28 GHz. The resultant frequency depends on the specific combination of the RF and the drive frequency of the MZM. Owing to the utilization of the DSF, where the zero-dispersion wavelength is in the vicinity of 1550 nm, the proposed design is capable of mitigating the fiber dispersion hence achieving an improved beamforming performance. We employed 4 elements per TAA for the sake of showing the benefits of beamforming.

In order to show that our proposed A-RoF system has a minimal impact on the BER performance compared to that of the conventional SM system, we transmit our mmWave signal over the wireless channel and then compare the performance of the two systems. The beamformed mmWave SM signal obtained after A-RoF transmission is impaired by the mmWave

wireless channel [16]. Figure 9 shows the BER performance of $(N_t \times N_r)$=(2×1), (2×2), (4×1), (4×2) and (4×4) MIMO systems operating both with and without A-RoF, while analogue beamforming is employed at the transmitter and receiver. Again, four-element TAAs are employed for attaining beamforming in our simulated system.

In the conventional electronic SM encoding scheme of Section II-A, the antenna selection is based on implicitly conveyed symbols. In our proposed system, we modulate the implicit symbol and the classically modulated symbol onto each side-band of the ODSB signal generated by the LDs of Figure 3.

Furthermore, we applied the implicit bits to a 2^L-PSK/QAM modulation scheme, where 2^L also represents the number of antenna elements, while the classic modulated bits on Binary Phase-Shift Keying (BPSK) format. Then, before feeding the antennas, the corresponding 2^L-PSK/QAM symbols are recovered and then the implicit bits will select the activated antenna transmitting the up-converted mmWave signals carrying the modulated BPSK symbols. Thus, the implicit bits of the 2-antenna SM scheme are carried in the left side-band of Figure 3 as a BPSK symbol, while for the 4-antenna case, they are modulated as QPSK. The bit rate of the classic BPSK modulated bits is 1 Gbps, while the BPSK implicit bits convey a bit rate of 1 Gbps, and the QPSK implicit bits support a bit rate of 2 Gbps, hence achieving a multiplexed bits rate of 2 Gbps for our 2-antenna SM and 3 Gbps for 4-antenna SM.

As shown in Figure 9, when no optical amplifier is used, the BER performance of our proposed system shows a slight degradation, which is caused by the fiber's attenuation, non-linearity and optical noise. This degradation can be readily mitigated by introducing an optical amplifier, as shown in the next section in the context of MS-STSK. **Moreover, in Figure 9, the BER performance of wireless systems dispensing with beamforming is shown, where a 6 dB SNR gain is achieved by beamforming using $N = 4$ antenna arrays.**

As observed in Figure 9, by employing lower-complexity remote radio heads, our proposed SM scheme shows a slight BER degradation in comparison to the conventional SM
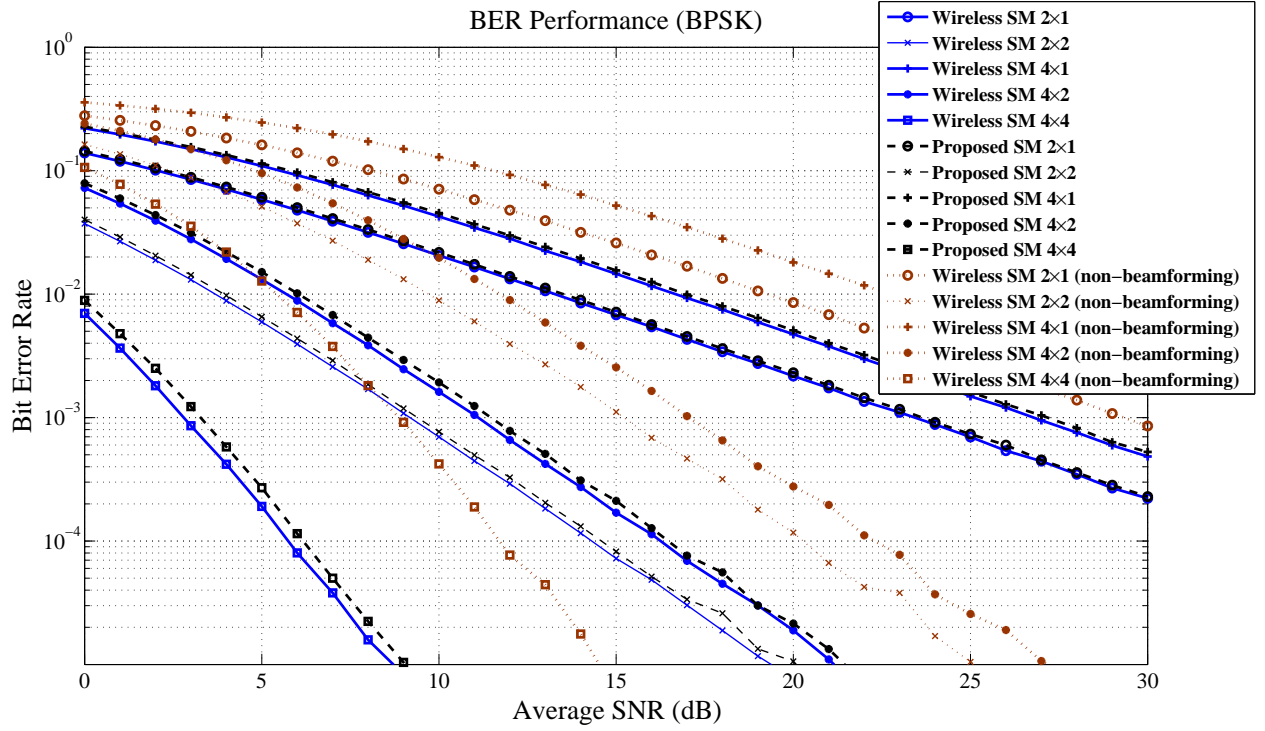
Figure 9: The BER performance of our SM scheme compared to that of the conventional electronic SM scheme using the parameters summarized in Table I.

scheme. In the following scheme, we incorporate MS-STSK into our system, which is a generalized architecture subsuming both SM and STSK.

III. A-RoF NETWORK DESIGN FOR MS-STSK

In this section, the MS-STSK scheme is intrinsically amalgamated with our A-RoF downlink combined with all-optical beamforming and upconversion to a mmWave frequency for transmission over the mmWave wireless channel.

A. Conventional MS-STSK Scheme

MS-STSK was proposed in [28] as a generalization of SM and STSK, where the data bit sequence is partitioned into three streams that convey the antenna selection, the dispersion matrix selection and the PSK/QAM modulated symbol. As shown in Figure 10, the data stream is divided into three parts: the bit stream B_1 is used for antenna selection, while the bit streams B_2 and B_3 are used for STSK encoding. In STSK encoding, $B_2 = log_2 Q$ bits are used for selecting one out of Q dispersion matrices, while B_3 is represented by the PSK/QAM symbol. The output of the STSK encoder is transmitted using N_{RF} RF chains, which are switched to a specific combination of N_{RF} out of the N_t antennas with the aid of the antenna selection unit. Hence, the B_1 and B_2 bit streams of Figure 10 are implicitly conveyed over the activated Antenna Combination (AC) index and the dispersion matrix selected, respectively.

The MS-STSK scheme is capable of utilising a compelling diversity and multiplexing trade-off [28]. As mentioned above, MS-STSK can be introduced into our system by imposing a slight extra complexity on the remote radio head compared to

the A-RoF-aided SM design of Figure 3. In this section, we denote the MS-STSK system as MS-STSK($N_t, M, N_r, T, Q, \mathcal{L}- PSK/QAM$), where each symbol is characterized in Table II. In the following section, we will discuss our A-RoF-aided MS-STSK design.

Table II: MS-STSK symbol notations

Parameter	Representation
N_t	Transmitter Antenna
M	STSK Space dimension
Nr	Receive antenna
Q	Number of dispersion matrix
T	STSK Time Slots
$\mathcal{L}$	PSK/QAM constellation size

B. Proposed A-RoF-aided MS-STSK design

The MS-STSK design is further extended and improved from the SM design proposed in Section II, as shown in Figure 11. Three changes have been made in the A-RoF aided MS-STSK system compared to the SM counterpart of Figure 3.

1) The x_1 implicit symbols carry the bits B_1 and B_2 of both the selected AC and of the dispersion matrix, rather than only of the antenna selection information of SM, which is mapped to the left-side band of the ODSB signals generated before the MZM of Figure 11. Here, the B_1 and B_2 bits are concatenated and then mapped to x_1.

2) If the number of implicit bits containing B_1 and B_2 is L_{MS}, then the symbols carrying the implicit bits would be mapped to $2^{L_{MS}} - PSK/QAM$ alphabet.
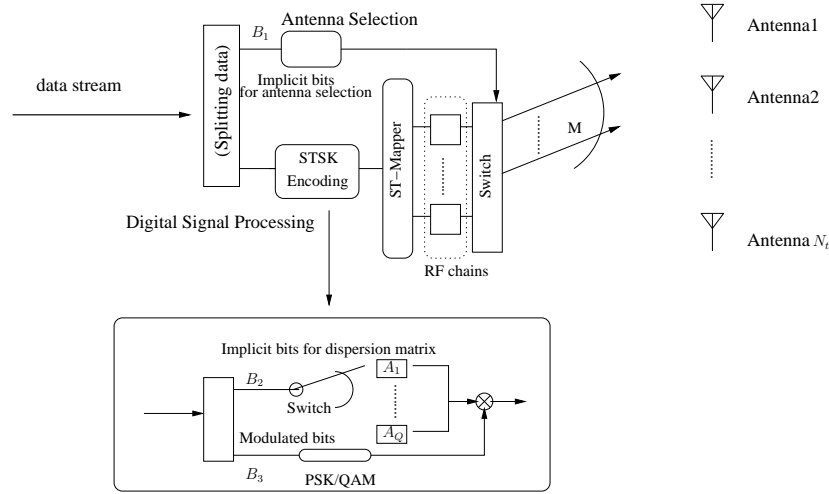
Figure 10: **Conventional electronic MS-STSK encoding scheme employed at the Base Stations of the conventional cellular architecture.**
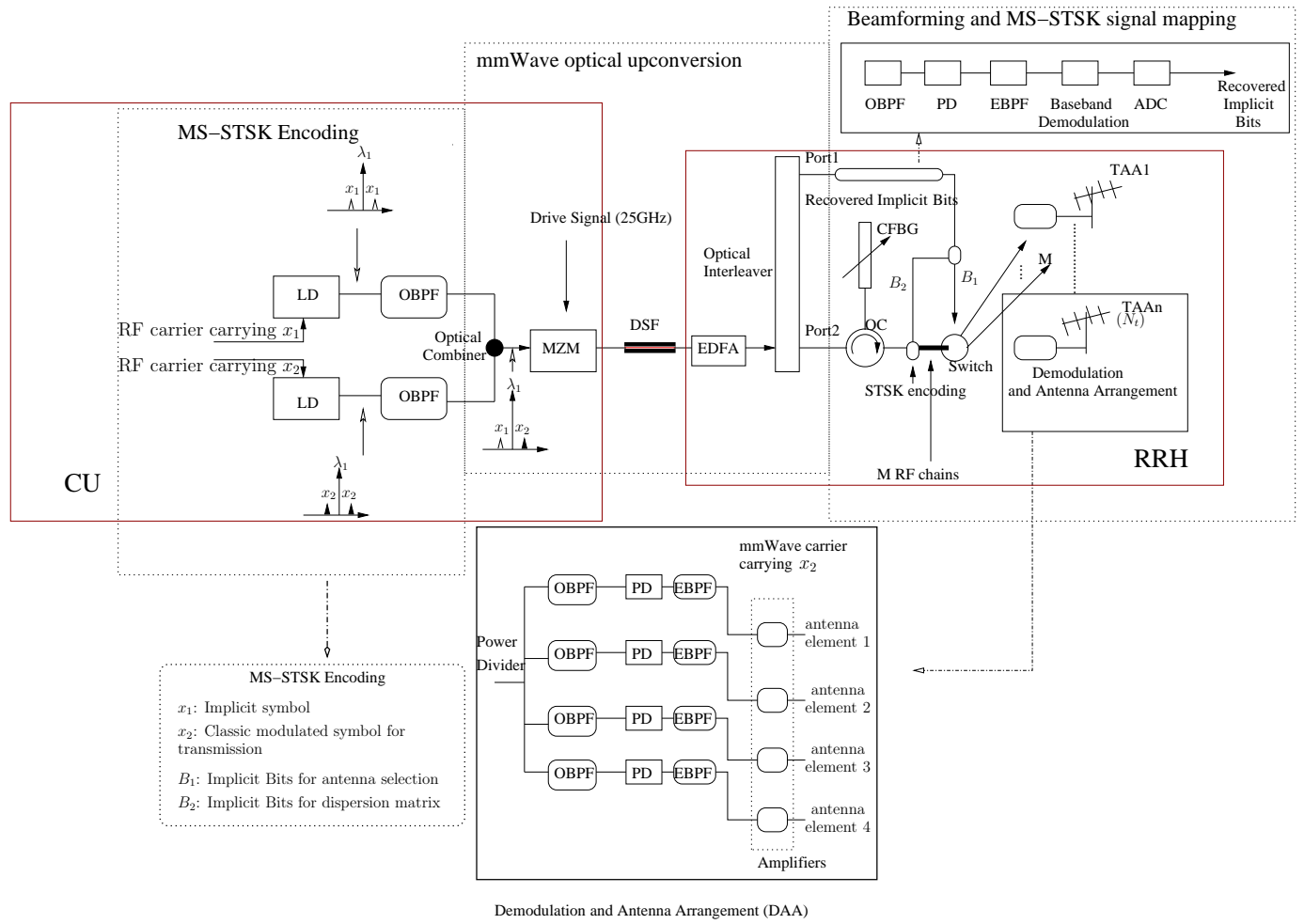
Figure 11: **A centralized A-RoF aided MS-STSK Network. The CU implements digital modulation, carrier modulation, E-O conversion and MS-STSK encoding, while the RRH carries out the radio functions (filtering, O-E conversion, photo-detection and amplifying radio transmission), as well as MS-STSK implicit data recovery and MS-STSK switching.**

Thus, the implicit bits convey both the information for antenna selection and the dispersion matrix selection. Hence, more implicit bits are conveyed by MS-STSK and therefore a larger constellation size is required to transmit the implicit bits of MS-STSK over the optical fiber, which is more susceptible to both fiber impairments and to optical noise. We invoked an Erbium-doped fiber amplifier (EDFA) before the OIL of Figure 11 in order to mitigate these effects by improving the optical SNR.

3) Furthermore, in the remote radio head of Figure 11, the recovered implicit bits are split into the B_1 and B_2 streams, which represent the antenna selection bits and the dispersion matrix selection bits, respectively. Then, the classic modulated symbol carried by the up-converted mmWave signal is multiplied by the dispersion matrix selected and then transmitted over the AC selected, while beamforming is introduced by CFBG, which was discussed in Section II.

Our A-RoF-aided MT-STSK scheme constitutes an extension of the A-RoF-aided SM scheme discussed in Section II. As shown in Figure 11, the ODSB modulated by x_1 and x_2 is up-converted to a mmWave frequency, and an optically aided beamforming scheme based on the CFBG philosophy of [36] is created. Thus, we adjusted the A-RoF network conceived for SM to include MS-STSK by adding a few extra components, such as an EDFA and the dispersion matrix selection scheme of Figure 11. Next, we present our simulation results and related discussion to verify our system.

C. System Simulation Results and Discussions

Table III: Simulation Parameters

Parameter	Value
Bit rate	5 Gbps (BPSK system)
	10 Gbps (16-QAM system)
RF signal	3 GHz
LD Center Wavelength	1550 nm
LD Power	0.1 mW
Drive Frequency (MZM)	25 GHz
Achieved mmWave frequency	28 GHz
MZM mode	push-pull mode
Fiber type	DSF
Fiber length	10 km
Channel Model	Split-Step Fourier Method
Modulation Type	BPSK/16QAM
EDFA Gain	20 dB
Wireless Channel	Rayleigh Fading Channel
Wireless Detection	ML Detection
Beamforming Type	4 Antenna Elements
Simulation Environment	MATLAB

Let us now consider an MS-STSK (4,2,2,2,4,BPSK) system based on the design depicted in Figure 11. The simulation parameters are shown in Table III. Due to the larger number of implicit bits of MS-STSK than that of our SM scheme, a higher order modulation scheme such as 16-QAM is required, which is more susceptible to fiber non-linearity. The LD power

is reduced to 0.1 milliWatt (mW) for the sake of mitigating the effect of non-linearity induced-phase shifts.

Before being mapped to the two side-bands of the ODSB scheme shown in Figure 11, the implicit bits used for the MS-STSK scheme of Figure 11 are mapped to the 16-QAM symbols x_1, where two bits are used for selection of a dispersion matrix and the other two bits are used for the antenna selection. Finally, the classic modulated symbols x_2 are BPSK symbols. Using the same data set for the dispersion matrix as in [28], Figure 12 shows the BER performance of conventional electronic MS-STSK **both with and without beamforming using** $N = 4$ **antenna arrays** and of our proposed A-RoF-aided MS-STSK system. The comparisons are based on (4×4), (4×2) and (4×1) MIMO schemes, where analogue beamforming using four antenna-elements is employed. It is clearly observed that there is only a minor BER degradation, when our fiber network is invoked. Moreover, recall from Figure 9, that without EDFA, there is still a modest degradation in BER performance. However, owing to the requirement of using a higher-order fiber-modulation for MS-STSK, which is more susceptible to fiber impairments, the proposed MT-STSK system relies on an EDFA having a 20 dB gain in order to compensate for the degradation. **Additionally, observe in Figure 12 that the beamforming aided system has a 6 dB beamforming gain.**

Furthermore, to verify that our system is scalable and suitable for high data rates, we mapped the classic modulated bits to a 16 QAMs while invoking another 16-QAM scheme for the implicit bits, transmitting a 10 Gbps signal using the same MT-STSK scheme as above. As discussed above, 16 QAM is more susceptible than BPSK to the fiber impairment, hence an EDFA of 26 dB gain is invoked. Figure 13 shows our comparison of the (4×4), (4×2) and (4×1) MS-MTSK MIMO schemes. Given that only a modest degradation is observed, we conclude that our SM/MS-STSK A-RoF network benefits from all-optical processing, whilst avoiding the ADC-and-DAC-related complexity in the remote radio head of Figure 11.

MT-STSK is a general scheme subsuming both SM and STSK, where space-time coding can be included, leading increased flexibility to our proposed system. Additionally, the beamforming solely relies on CFBG and the corresponding wavelengths, as discussed in Section II.

IV. CONCLUSIONS

In this paper, we presented a A-RoF aided SM/MS-STSK downlink network, where SM and MS-STSK are implemented in a centralized processing fashion. This design is capable of substantially reducing the complexity of the remote radio head, when intrinsically amalgamated with SM or MS-STSK. Our SM/MS-STSK design is capable of achieving optical up-conversion to mmWave carriers, whilst supporting optical fiber aided beamforming. Additionally, we achieved a bit rate of 10 Gbps for 16QAM and 10 km DSF in our MS-STSK fiber based A-RoF network, where the BER performance shows little degradation compared to those without fiber networks.

REFERENCES

[1] L. Hanzo, M. El-Hajjar, and O. Alamri, "Near-capacity wireless transceivers and cooperative communications in the MIMO era: Evolution
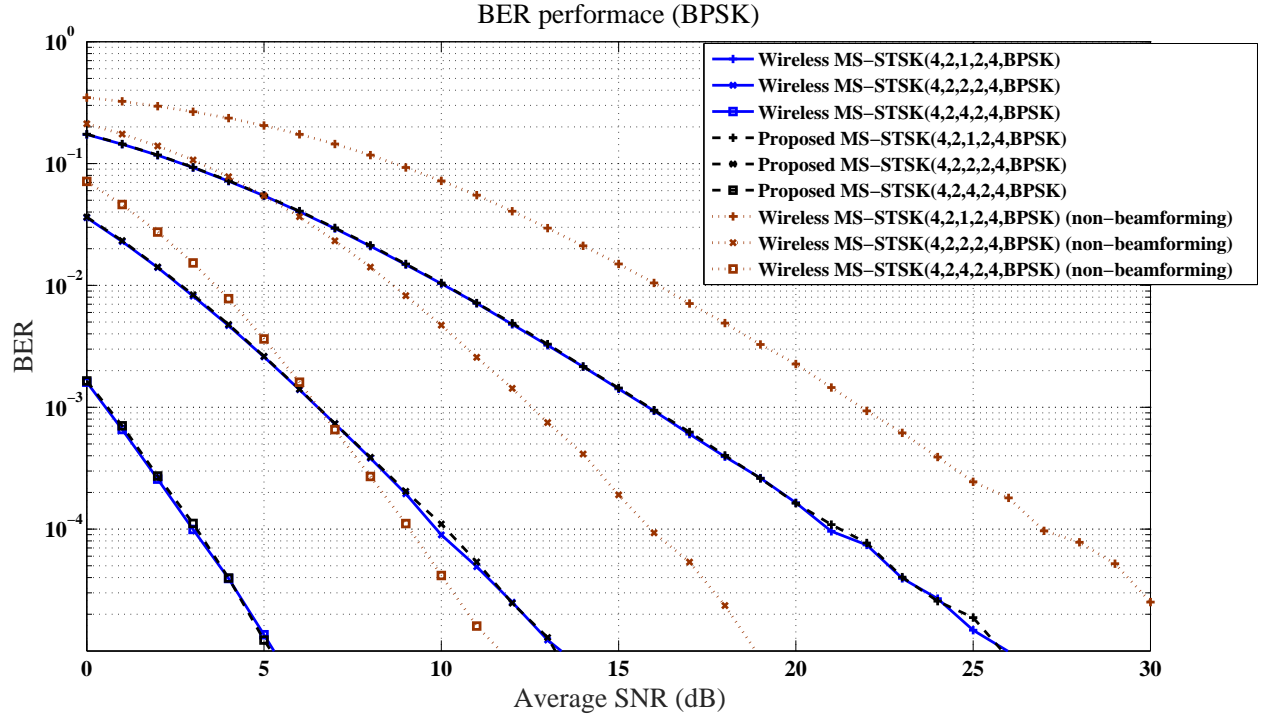
Figure 12: BER performance of conventional electronic MS-STSK and of our proposed MS-STSK scheme for 5Gbps BPSK modulated signal using the parameters summarised in Table III.
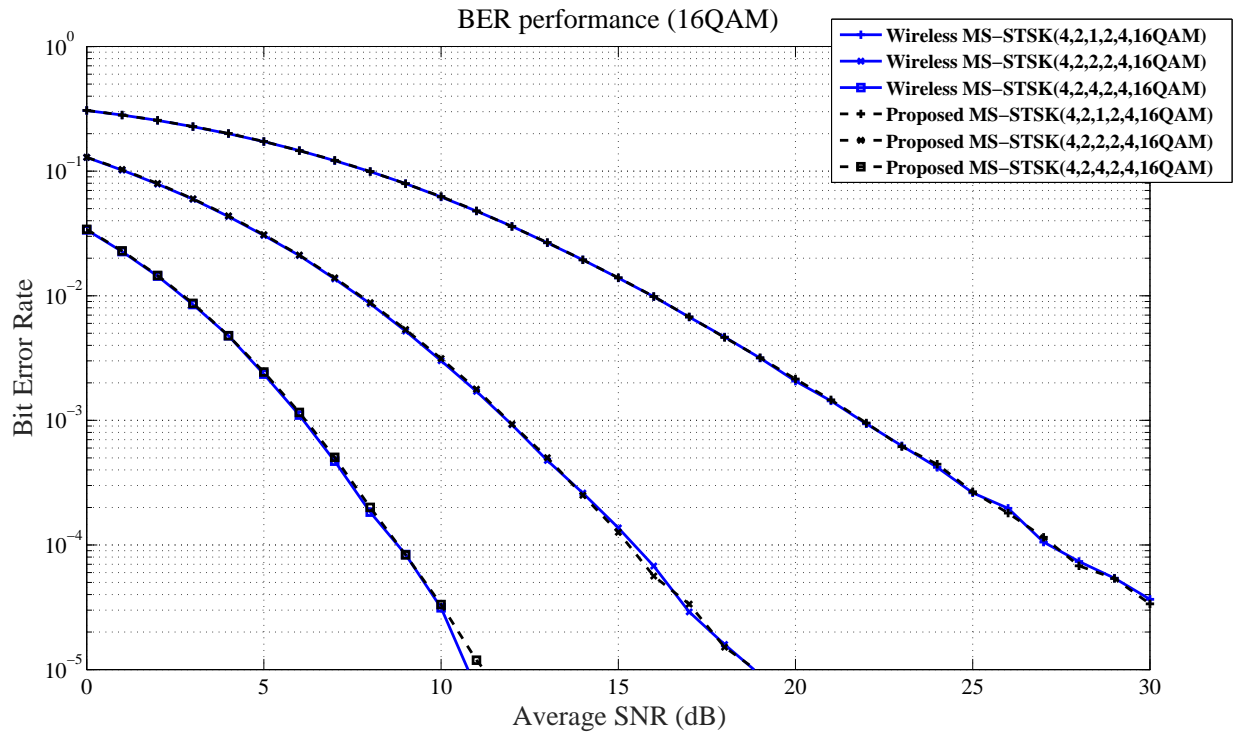

Figure 13: BER performance of conventional electronic MS-STSK and of our proposed MS-STSK scheme for 10Gbps 16 QAM using the parameters summarised in Table III.

of standards, waveform design, and future perspectives," *Proceedings of the IEEE*, vol. 99, pp. 1343–1385, Aug 2011.

[2] A. Goldsmith, *Wireless communications*. Cambridge university press, 2005.

[3] L. Hanzo, H. Haas, S. Imre, D. O'Brien, M. Rupp, and L. Gyongyosi, "Wireless myths, realities, and futures: from 3G/4G to optical and quantum wireless," *Proceedings of the IEEE*, vol. 100, no. Special Centennial Issue, pp. 1853–1888, 2012.

[4] S. Rangan, T. S. Rappaport, and E. Erkip, "Millimeter-wave cellular wireless networks: Potentials and challenges," *Proceedings of the IEEE*, vol. 102, pp. 366–385, March 2014.

[5] V. Thomas, M. El-Hajjar, and L. Hanzo, "Performance improvement and cost reduction techniques for radio over fiber communications," *IEEE Communications Surveys Tutorials*, vol. 17, pp. 627–670, Second quarter 2015.

[6] J. M. B. Oliveira, H. M. Salgado, and M. R. D. Rodrigues, "A new mse channel estimator optimized for nonlinearly distorted faded OFDM signals with applications to radio over fiber," *IEEE Transactions on Communications*, vol. 62, pp. 2977–2985, Aug 2014.

[7] D. Novak, R. B. Waterhouse, A. Nirmalathas, C. Lim, P. A. Gamage, T. R. Clark, M. L. Dennis, and J. A. Nanzer, "Radio-over-fiber technologies for emerging wireless systems," *IEEE Journal of Quantum Electronics*, vol. 52, pp. 1–11, Jan 2016.

[8] S. Z. Pinter and X. N. Fernando, "Estimation and equalization of fiber-wireless uplink for multiuser CDMA 4G networks," *IEEE Transactions on Communications*, vol. 58, pp. 1803–1813, June 2010.

[9] A. Checko, H. L. Christiansen, Y. Yan, L. Scolari, G. Kardaras, M. S. Berger, and L. Dittmann, "Cloud RAN for mobile networks——a technology overview," *IEEE Communications Surveys Tutorials*, vol. 17, pp. 405–426, Firstquarter 2015.

[10] M. Peng, K. Zhang, J. Jiang, J. Wang, and W. Wang, "Energy-efficient resource assignment and power allocation in heterogeneous cloud radio access networks," *IEEE Transactions on Vehicular Technology*, vol. 64, pp. 5275–5287, Nov 2015.

[11] V. N. Ha, L. B. Le, and N. D. Dao, "Coordinated multipoint transmission design for cloud RANs with limited fronthaul capacity constraints," *IEEE Transactions on Vehicular Technology*, vol. 65, pp. 7432–7447, Sept 2016.

[12] M. Peng, C. Wang, V. Lau, and H. V. Poor, "Fronthaul-constrained cloud radio access networks: Insights and challenges," *IEEE Wireless Communications*, vol. 22, no. 2, pp. 152–160, 2015.

[13] Y. Li, M. El-Hajjar, and L. Hanzo, "Joint space-time block-coding and beamforming for the multi-user radio over plastic fiber downlink," *IEEE Transactions on Vehicular Technology*, vol. PP, no. 99, pp. 1–1, 2017.

[14] A. Checko, H. L. Christiansen, Y. Yan, L. Scolari, G. Kardaras, M. S. Berger, and L. Dittmann, "Cloud RAN for mobile networks-a technology overview," *IEEE Communications surveys and tutorials*, vol. 17, no. 1, pp. 405–426, 2015.

[15] G. S. D. Gordon, M. J. Crisp, R. V. Penty, and I. H. White, "Experimental evaluation of layout designs for 3 × 3 MIMO-enabled radio-over-fiber distributed antenna systems," *IEEE Transactions on Vehicular Technology*, vol. 63, pp. 643–653, Feb 2014.

[16] T. Rappaport, S. Sun, R. Mayzus, H. Zhao, Y. Azar, K. Wang, G. Wong, J. Schulz, M. Samimi, and F. Gutierrez, "Millimeter wave mobile communications for 5G cellular: it will work!," *Access, IEEE*, vol. 1, pp. 335–349, 2013.

[17] V. A. Thomas, M. El-Hajjar, and L. Hanzo, "Millimeter-wave radio over fiber optical upconversion techniques relying on link nonlinearity," *IEEE Communications Surveys Tutorials*, vol. 18, pp. 29–53, First quarter 2016.

[18] Y. Xiang, C. Chen, C. Zhang, and K. Qiu, "Wired/wireless access integrated RoF-PON with scalable generation of multi-frequency MMWs enabled by polarization multiplexed FWM in SOA," *Optics express*, vol. 21, no. 1, pp. 1218–1225, 2013.

[19] C. Zhang, L. Wang, and K. Qiu, "Proposal for all-optical generation of multiple-frequency millimeter-wave signals for RoF system with multiple base stations using FWM in SOA," *Optics express*, vol. 19, no. 15, pp. 13957–13962, 2011.

[20] Y. Xiang, N. Jiang, C. Chen, C. Zhang, and K. Qiu, "Wired/wireless access integrated RoF-PON with scalable generation of multi-frequency MMWs enabled by tunable optical frequency comb," *Optics Express*, vol. 21, no. 17, pp. 19762–19767, 2013.

[21] C. Zhang, C. Chen, and K. Qiu, "Hybrid bidirectional radio-over-fiber-based orthogonal frequency division multiple access-passive optical network supporting 60/120 ghz using offset quadrate phase shift keying," *Optical Engineering*, vol. 54, no. 9, p. 096108, 2015.

[22] Z. Cao, Q. Ma, A. B. Smolders, Y. Jiao, M. J. Wale, C. W. Oh, H. Wu, and A. M. J. Koonen, "Advanced integration techniques on broadband millimeter-wave beam steering for 5G wireless networks and beyond," *IEEE Journal of Quantum Electronics*, vol. 52, no. 1, pp. 1–20, 2016.

[23] M. D. Renzo, H. Haas, A. Ghrayeb, S. Sugiura, and L. Hanzo, "Spatial modulation for generalized MIMO: Challenges, opportunities, and implementation," *Proceedings of the IEEE*, vol. 102, pp. 56–103, Jan 2014.

[24] R. Y. Mesleh, H. Haas, S. Sinanovic, C. W. Ahn, and S. Yun, "Spatial modulation," *IEEE Transactions on Vehicular Technology*, vol. 57, pp. 2228–2241, July 2008.

[25] C. X. Wang, F. Haider, X. Gao, X. H. You, Y. Yang, D. Yuan, H. M. Aggoune, H. Haas, S. Fletcher, and E. Hepsaydir, "Cellular architecture and key technologies for 5G wireless communication networks," *IEEE Communications Magazine*, vol. 52, pp. 122–130, February 2014.

[26] S. Sugiura, S. Chen, and L. Hanzo, "A universal space-time architecture for multiple-antenna aided systems," *IEEE Communications Surveys Tutorials*, vol. 14, pp. 401–420, Second quarter 2012.

[27] S. Sugiura, S. Chen, and L. Hanzo, "Coherent and differential space-time shift keying: A dispersion matrix approach," *IEEE Transactions on Communications*, vol. 58, pp. 3219–3230, November 2010.

[28] I. A. Hemadeh, M. El-Hajjar, S. Won, and L. Hanzo, "Multi-set space-time shift-keying with reduced detection complexity," *IEEE Access*, vol. 4, pp. 4234–4246, 2016.

[29] T. Erdogan, "Fiber grating spectra," *Journal of lightwave technology*, vol. 15, no. 8, pp. 1277–1294, 1997.

[30] G. P. Agrawal, *Fiber-optic communication systems*, vol. 222. John Wiley & Sons, 2012.

[31] H. Chettat, L. M. Simohamed, Y. Bouslimani, and H. Hamam, "RoF networks : A comprehensive study," in *2008 3rd International Symposium on Wireless Pervasive Computing*, pp. 495–498, May 2008.

[32] M. El-Hajjar and L. Hanzo, "Multi-functional MIMO systems: A combined diversity and multiplexing design perspective," *IEEE Wireless Communications*, vol. 17, pp. 73–79, April 2010.

[33] S. Ghafoor and L. Hanzo, "Reduced dispersion duplex DQPSK radio-over-fiber communications using single-laser-based multiple sidebands," in *2011 IEEE International Conference on Communications (ICC)*, pp. 1–5, June 2011.

[34] J. Corral, J. Marti, S. Regidor, J. Foster, R. Laming, and M. Cole, "Continuously variable true time-delay optical feeder for phased-array antenna employing chirped fiber grating," *IEEE Transactions on Microwave Theory and Techniques*, vol. 45, no. 8, pp. 1531–1536, 1997.

[35] J. Yao, J. Yang, and Y. Liu, "Continuous true-time-delay beamforming employing a multiwavelength tunable fiber laser source," *IEEE Photonics Technology Letters*, vol. 14, pp. 687–689, May 2002.

[36] Y. Liu, J. Yang, and J. Yao, "Continuous true-time-delay beamforming for phased array antenna using a tunable chirped fiber grating delay line," *IEEE Photonics Technology Letters*, vol. 14, pp. 1172–1174, Aug 2002.

[37] A. Alkhateeb, O. E. Ayach, G. Leus, and R. W. Heath, "Channel estimation and hybrid precoding for millimeter wave cellular systems," *IEEE Journal of Selected Topics in Signal Processing*, vol. 8, pp. 831–846, Oct 2014.

[38] C. Zhang, D. Guo, and P. Fan, "Tracking angles of departure and arrival in a mobile millimeter wave channel," in *2016 IEEE International Conference on Communications (ICC)*, pp. 1–6, May 2016.

[39] I. A. Hemadeh, M. El-Hajjar, and L. Hanzo, "Hierarchical multi-functional layered spatial modulation," *IEEE Access*, 2018.

Yichuan Li received B.Sc. degree in Optics Information Science and Technology from China University of Petroleum (East China), Qingdao, China, in 2012, and M.Sc. degree in wireless communications from the University of Southampton, Southampton, UK., in 2014. He was a research assistant in the Lightwave Communication Lab of the Chinese University of Hong Kong from July to October in 2017. Currently, he is working toward the Ph.D. degree with the University of Southampton. His research is focused on the the radio over fiber for backhaul, front-haul and indoor communication network. His research interests are millimeter wave over fiber, optical fiber aided analogue beamforming techniques, Multifunctional MIMO and mode division multiplexing in multimode fiber (both glass multimode fiber and plastic optical fiber).

Ibrahim A. Hemadeh received a B.Eng. degree (with first class honours) in Computer and Communications Engineering from the Islamic University of Lebanon, Lebanon, in 2010. He then received an M.Sc. degree in Wireless Communications (with distinction) and a Ph.D. degree in Electronics and Electrical Engineering from the University of Southampton, UK, in 2012 and 2017, respectively. He is currently a postdoctocal researcher at Southampton Wireless (SW) group, University of Southampton, UK. His research interests mainly include millimeter-wave communications, multi-functional MIMO, multi-dimensional (time-space-and frequency) transceiver designs, channel coding as well as multi-user MIMO.

Mohammed El-Hajjar is an Associate Professor in the Department of Electronics and Computer Science in the University of Southampton. He received his PhD in Wireless Communications from the University of Southampton, UK in 2008. Following the PhD, he joined Imagination Technologies as a design engineer, where he worked on designing and developing Imagination's multi-standard communications platform, which resulted in three patents. He is the recipient of several academic awards and has published a Wiley-IEEE book and in excess of 80 journal and conference papers. Mohammed's research interests include the development of intelligent communications systems, energy-efficient transceiver design, MIMO, millimeter wave communications and Radio over fiber network design.

Lajos Hanzo (http://www-mobile.ecs.soton.ac.uk) FREng, FIEEE, FIET, Fellow of EURASIP, DSc received his degree in electronics in 1976 and his doctorate in 1983. In 2009 he was awarded an honorary doctorate by the Technical University of Budapest and in 2015 by the University of Edinburgh. In 2016 he was admitted to the Hungarian Academy of Science. During his 40-year career in telecommunications he has held various research and academic posts in Hungary, Germany and the UK. Since 1986 he has been with the School of Electronics and Computer Science, University of Southampton, UK, where he holds the chair in telecommunications. He has successfully supervised 111 PhD students, co-authored 18 John Wiley/IEEE Press books on mobile radio communications totalling in excess of 10 000 pages, published 1600+ research contributions at IEEE Xplore, acted both as TPC and General Chair of IEEE conferences, presented keynote lectures and has been awarded a number of distinctions. Currently he is directing a 60-strong academic research team, working on a range of research projects in the field of wireless multimedia communications sponsored by industry, the Engineering and Physical Sciences Research Council (EPSRC) UK, the European Research Council's Advanced Fellow Grant and the Royal Society's Wolfson Research Merit Award. He is an enthusiastic supporter of industrial and academic liaison and he offers a range of industrial courses. He is also a Governor of the IEEE VTS. During 2008 - 2012 he was the Editor-in-Chief of the IEEE Press and a Chaired Professor also at Tsinghua University, Beijing. For further information on research in progress and associated publications please refer to http://www-mobile.ecs.soton.ac.uk Lajos has 30 000+ citations and an H-index of 70.